Journal Name

ARTICLE

Synthesis and characterisation of new Bi(III)-containing apatite-type oxide ion conductors: the influence of lone pairs

M. L. Tate,[a, b] C. A. Fuller,[a] M. Avdeev,[b] H. E. A. Brand[c] , G. J. McIntyre[b] and I. Radosavljevic Evans[a,*]

Lone-pair cations are known to enhance oxide ion conductivity in fluorite- and Aurivillius-type materials. Among the apatite-type phases, the opposite trend is found for the more widely studied silicate oxide ion conductors, which exhibit a dramatic decrease in conductivity on Bi(III) incorporation. In this work, the influence of lone-pair cations on the properties of apatite-type germanate oxide ion conductors has been investigated by preparing and characterising seven related compositions with varying Bi(III) content, by X-ray and neutron powder diffraction and impedance spectroscopy. All materials are very good oxide ion conductors (with conductivities of up to 1.29×10^{-2} at 775ºC). Increasing Bi(III) content leads to increases in conductivity by up to an order of magnitude, suggesting significant differences in the oxide-ion conduction mechanisms between lone-pair containing apatite-type germanate and silicate solid electrolytes.

Introduction

Apatite-type germanates and silicates of the general formula $A_{10}(TO_4)_6O_{2\pm\delta}$, (A = alkaline or rare earth, Pb, Bi etc.; T = Ge, Si) display high oxide ion conductivities in the so-called intermediate-temperature solid oxide fuel cell (IT-SOFC) region between 450 and 600 ºC.[1-12] There has been considerable research effort to understand the oxide ion conductivity mechanisms and, on this basis, optimise the composition and properties of these materials.[13-16] The number and locations of any interstitial oxide ions are crucial for the conductivity, and are still debated in the literature.[7, 13-25]

Another important aspect of the structure-property relationships in apatite solid electrolytes is the influence of lone-pair cations. In several different families of materials, most notably in fluorite- and Aurivilius-type phases, lone pairs are thought to enhance conductivity by providing a highly polarisable cation sublattice for the oxide ions to hop through.[26-30] The effect of potential Bi(III)-doping on oxide ion conductivity in apatites is presumed to be detrimental, due to assumption that the lone pairs are located so that they point towards the centre of the channel in the apatite structure, and suppress the O^{2-} mobility within the channel. However, there are relatively few Bi(III)-containing apatites reported in the literature, and even fewer reports of oxide ion conductivity measurements. Zhuravlev *et al.* reported the preparation of three phases in the $Bi_2Ca_{8-2x}La_{2x}[(VO_4)_{6-2x}(GeO_4)_{2x}]O_2$ (x = 1, 2, 3) series without any physical property measurements. [31] More recently, we reported the synthesis and characterisation of

$Bi_2La_8[(GeO_4)_6]O_3$, a triclinic apatite which undergoes a reversible phase transition into the hexagonal structure near 680ºC and reaches oxide ion conductivity the same as that of yttria-stabilised zirconia at 800ºC. [32]

In this work, we report the preparation and characterisation of a series of lone-pair-containing apatite-type materials with varying Bi(III) content by powder diffraction methods (laboratory X-ray diffraction, synchrotron X-ray diffraction, neutron diffraction) and conductivity measurements.

Experimental

Sample preparation

All samples were prepared by conventional solid state synthesis. The reagents used were: Bi_2O_3 (Sigma-Aldrich, 99.90%), $CaCO_3$ (BDH, 99.50%), GeO_2 (Sigma-Aldrich, 99.99%), La_2O_3 (Sigma-Aldrich, 99.99%) and V_2O_5 (Sigma-Aldrich, 99.99%). Prior to use as a reagent, La_2O_3 was heated at 1000 °C. The synthesis temperature was 1100 °C and heating durations were between 18 and 54 hours, with heating and cooling rates of 5 °C per minute.

Characterisation

Room-temperature powder X-ray diffraction (PXRD) data were collected on a Bruker AXS D8 Advance diffractometer with Cu Kα radiation and a Lynx-Eye detector. Synchrotron PXRD data were collected on the Powder Diffraction Beamline at the Australian Synchrotron.[33] The samples were finely ground and placed into 0.2 mm diameter quartz capillaries which were rotated during data collection. Data were collected in a 2θ range of 3 to 83 ° using a monochromated X-ray beam (λ = 0.6354 Å, calibrated against NIST SRM660b LaB_6) and a Mythen II microstrip detector. Each data set was collected with the detector in two different positions offset by 0.5 ° to cover gaps

[a.] Durham University, Department of Chemistry, Science Site, South Road, Durham, DH1 3LE, UK. *ivana.radosavljevic@durham.ac.uk
[b.] Australian Nuclear Science and Technology Organisation, Lucas Heights NSW 2234, Australia.
[c.] Australian Synchrotron, 800 Blackburn Road, Clayton VIC 3168, Australia.

in the angular range of the modular detector strip, with a collection time of 900 seconds per position. The two collected data sets were then combined into a single diffraction pattern using the PDViPeR software. Neutron diffraction data were collected on the ECHIDNA powder neutron diffractometer on the OPAL reactor at ANSTO.[34] For each data collection, approximately 8 g of powdered sample was placed into a 9 mm diameter vanadium can and data were collected over the 2θ range of 6 to 164 °, with the wavelength of the neutrons fixed at 2.4395(5) Å using the [331] reflection of a Ge monochromator. No additional collimation was applied. All powder diffraction data were analysed using the Topas Academic software.[35]

AC impedance spectroscopy measurements were carried out in air using a Solartron 1260 frequency response analyser over a 10^6 to 10^{-1} Hz frequency range. The circular faces of the sintered pellet were coated with a fine layer of Pt paste and affixed in a Probostat A-6 measurement cell. The coated pellets were fired at 800°C for 1 hr to eliminate the organic components from the paste to form electrodes. The impedance data were collected on heating in temperature intervals of 50 °C for all samples except for $Bi_2La_8[(GeO_4)_6]O_3$, for which a temperature step of 25 °C was used, with a heating rate of 5 °C/min. Before data collection, the pellet was thermally stabilised for 45 mins. The complex impedance data were analysed using the Zview 3.0a software package.

Results and discussion

Structural characterisation

$Bi_2Ca_6La_2[(VO_4)_4(GeO_4)_2]O_2$, $Bi_2Ca_4La_4[(VO_4)_2(GeO_4)_4]O_2$, and $Bi_2Ca_2La_6[(GeO_4)_6]O_2$ were previously characterised by PXRD and Raman spectroscopy.[31] In the absence of any additional (synchrotron, neutron) diffraction data on these materials, and we used PXRD and the Rietveld method[36] (using the previously published models) only to confirm the preparation of single-phase materials suitable for physical property measurements. The Rietveld fits obtained shown in Fig. 1 demonstrate this.
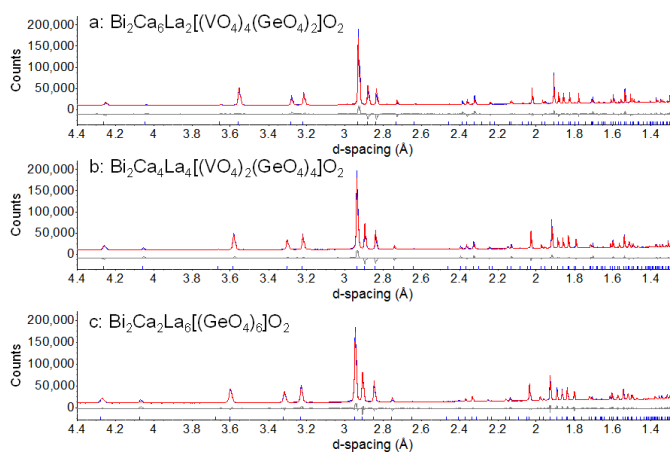

Fig. 1: Rietveld refinements for: a) $Bi_2Ca_6La_2[(VO_4)_4(GeO_4)_2]O_2$, a = 9.8378(1) Å, c = 7.1196(1) Å, R_{wp} = 4.128 %; b) $Bi_2Ca_4La_4[(VO_4)_2(GeO_4)_4]O_2$, a = 9.8473(1) Å, c = 7.1709(1) Å, R_{wp} = 3.671 %; c) $Bi_2Ca_2La_6[(GeO_4)_6]O_2$, a = 9.8758(1) Å, c = 7.2084(1) Å, R_{wp} = 2.867 %.

Laboratory PXRD data collected at room temperature on new materials $Bi_4Ca_4La_2[(VO_4)_2(GeO_4)_4]O_2$ and $Bi_4Ca_2La_4[(GeO_4)_6]O_2$, analysed by the Rietveld method using modified versions of the structural model reported by León-Reina et al. for $La_{9.5}[(GeO_4)_{5.5}(AlO_4)_{0.5}]O_2$ (space group $P6_3/m$),[13] confirmed that these new materials adopted hexagonal structures. A more detailed structural characterisation was then carried out using synchrotron PXRD and PND data. The starting model for the refinements was the hexagonal form of $Bi_2La_8[(GeO_4)_6]O_3$, albeit with the interstitial oxygen content removed and the metal content initially split equally across all relevant sites according to the stoichiometry of the material. For each composition, a combined refinement of the synchrotron PXRD and PND data sets was undertaken with the following parameters refined: background, lattice parameters, independent isotropic temperature factors for each crystallographic site, all atomic coordinates, metal-site occupancies, scale factors, peak-shape terms (PND) and size-strain terms (synchrotron PXRD). The metal site occupancies were restrained to maintain the correct overall stoichiometry, but were allowed to refine freely across the A1 and A2 sites. The $Bi_4Ca_4La_2[(VO_4)_2(GeO_4)_4]O_2$ sample contains a small percentage of $Bi_4V_2O_{11}$, and so two lattice parameters and one overall isotropic temperature factor were refined for this impurity phase, whilst $Bi_4Ca_2La_4[(GeO_4)_6]O_2$ contains a small amount of Bi_2GeO_5, so three lattice parameters and one overall isotropic temperature factor were refined for this phase. The structural parameters obtained are given in Tables 1 and 2 and the final fits to the data sets are presented in Fig. 2.
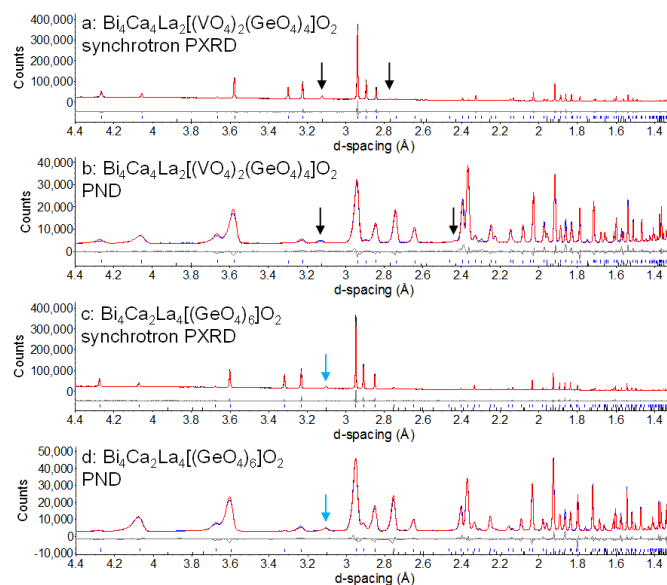

Fig. 2: Rietveld fits for $Bi_4Ca_4La_2[(VO_4)_2(GeO_4)_4]O_2$ (a = 9.84710(5) Å, c = 7.15231(4) Å) at room temperature to: a) synchrotron PXRD data, R_{wp} = 4.642 %; b) PND data, R_{wp} = 5.755 %. The peak positions for the $Bi_4V_2O_{11}$ impurity phase are denoted with black tick marks and the impurity peaks with black arrows. Rietveld fits for $Bi_4Ca_2La_4[(GeO_4)_6]O_2$ (a = 9.86970(4) Å, c = 7.19700(4) Å) at room temperature to: c) synchrotron PXRD data, R_{wp} = 4.804 %; d) PND data, R_{wp} = 7.490 %. The peak positions for the Bi_2GeO_5 impurity phase are denoted with black tick marks and the impurity peaks with blue arrows.

Table 1: Crystallographic data for hexagonal $Bi_4Ca_4La_2[(VO_4)_2(GeO_4)_4]O_2$ at 30 °C. Space group P6$_3$/m, a = 9.84710(5) Å, c = 7.15231(4) Å, V = 600.612(7) Å^3.

Site	Atom	x	y	z	Occ	B_{iso} (Å^2)
A1	Ca	1/3	2/3	0.4889(3)	0.80(1)	1.19(6)
A1	Bi	1/3	2/3	0.4889(3)	0.204(4)	1.19(6)
A2	La	0.2354(1)	0.0060(2)	1/4	0.33(1)	2.04(3)
A2	Ca	0.2354(1)	0.0060(2)	1/4	0.13(1)	2.04(3)
A2	Bi	0.2354(1)	0.0060(2)	1/4	0.533(6)	2.04(3)
T1	Ge	0.4002(2)	0.3779(2)	1/4	2/3	0.48(3)
T1	V	0.4002(2)	0.3779(2)	1/4	1/3	0.48(3)
O1	O	0.3241(2)	0.4966(2)	1/4	1	0.79(5)
O2	O	0.6034(2)	0.4687(2)	1/4	1	1.50(5)
O3	O	0.3329(2)	0.2442(2)	0.0678(2)	1	2.11(4)
O4	O	0	0	1/4	1	5.1(1)

Table 2: Crystallographic data for hexagonal $Bi_4Ca_2La_4[(GeO_4)_6]O_2$ at 30 °C. Space group P6$_3$/m, a = 9.86970(4) Å, c = 7.19700(4) Å, V = 607.142(6) Å^3.

Site	Atom	x	y	z	Occ	B_{iso} (Å^2)
A1	La	1/3	2/3	0.4917(3)	0.31(1)	1.46(6)
A1	Ca	1/3	2/3	0.4917(3)	0.50(1)	1.46(6)
A1	Bi	1/3	2/3	0.4917(3)	0.20(1)	1.46(6)
A2	La	0.2349(1)	0.0019(2)	1/4	0.46(1)	1.61(4)
A2	Bi	0.2349(1)	0.0019(2)	1/4	0.54(1)	1.61(4)
T1	Ge	0.4022(2)	0.3773(1)	1/4	1	0.45(3)
O1	O	0.3224(2)	0.4968(2)	1/4	1	0.85(5)
O2	O	0.6043(2)	0.4709(2)	1/4	1	2.08(6)
O3	O	0.3350(2)	0.2440(2)	0.0663(2)	1	2.60(4)
O4	O	0	0	1/4	1	5.4(1)

The structures of these two materials is similar to that of the hexagonal $Bi_2La_8[(GeO_4)_6]O_3$: a framework of $[(A1)_4][(TO_4)_6]$ surrounding $(A2)_6O_2$ units (A = Bi/Ca/La, T = V/Ge), with the Bi atoms favouring the channel site (A2) predominantly, whilst the Ca atoms prefer the framework site (A1), Fig. 2. The same site preferences were observed in the structure of $Bi_2Ca_8[(VO_4)_6]O_2$, determined from single-crystal diffraction data, which shows Bi favouring the channel site whilst the Ca atoms occupy primarily the framework sites.[37]
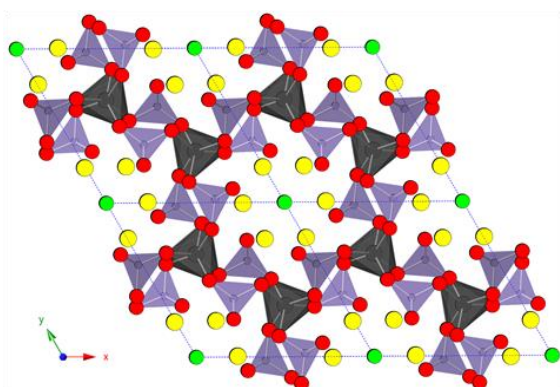

Fig. 3: The $[A1]_4[A2]_6[(TO_4)_6][O_2]$ apatite structure viewed along the z axis. Black = framework A1 sites, yellow = channel A2 sites, red = framework O, green = channel O. Bonds to the A2 and the channel O sites have been omitted for clarity.

Table 3: Bond valence sums for $Bi_4Ca_2La_4[(GeO_4)_6]O_2$ and $Bi_4Ca_4La_2[(VO_4)_2(GeO_4)_4]O_2$. The values in square brackets are those expected for the site based on the ratio of M^{2+} and M^{3+} cations.

$Bi_4Ca_2La_4[(GeO_4)_6]O_2$		$Bi_4Ca_4La_2[(VO_4)_2(GeO_4)_4]O_2$	
Site	Valence	Site	Valence
A1	2.36(1) [2.53]	A1	2.03(1) [2.25]
A2	2.68(1) [3.00]	A2	2.62(1) [2.87]
T1	4.16(1) [4.00]	T1	4.57(2) [4.33]

Bond valence sums calculated for these materials (Table 3) are consistent with our previous finding, based on $Bi_2La_8[(GeO_4)_6]O_3$, that there is not a simple relationship between the bonding requirements expressed through bond valence sums, and symmetry lowering in apatites, at least for the Bi(III)-containing phases.[32] Relative to the bond valence sums expected, the A-sites are under-bonded and the T-sites over-bonded both in $Bi_4Ca_2La_4[(GeO_4)_6]O_2$ and $Bi_4Ca_4La_2[(VO_4)_2(GeO_4)_4]O_2$, and yet, both materials are hexagonal instead of distorting into triclinic structures to alleviate this. Our on-going X-ray and neutron total scattering experiments and pair distribution function analysis of a series of germanates adopting structures belonging to different crystal systems is expected to provide a local structure based understanding of the symmetry lowering in apatite-type functional materials.

Conductivity measurements

The complex impedance spectra for all samples show a single large semi-circular arc attributed to bulk response at low temperatures, with Warburg-type electrode responses observed at frequencies below 10 Hz. A parallel resistor-capacitor model was used to treat the bulk responses, and the grain boundary and bulk responses could not be separated at high frequencies in the large impedance arc.
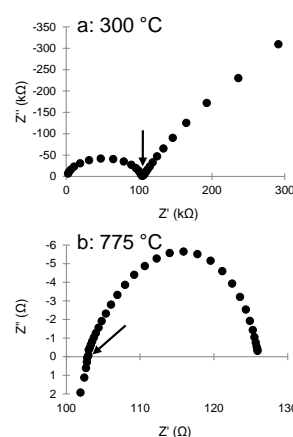
Fig. 4: Nyquist plots showing the impedance curves for $Bi_4Ca_4La_2[(VO_4)_2(GeO_4)_4]O_2$ at a) 300 °C; b) 775 °C.

The low-frequency intercepts of the semi-circular arcs arise from the bulk resistivities of the samples (marked in Fig. 4a), with capacitances calculated using ωRC = 1 at 300 °C ranging between 2.20 and 4.79 pFcm^{-1} for the six materials studied,

which are consistent with bulk responses. Below 10 Hz, the calculated capacitances from the Warburg-type responses are between 10^{-7} and 10^{-5} Fcm^{-1}, indicating ionic conduction.[38] At high temperatures the bulk responses disappear, resulting in a single observable arc forming, and so the total resistivities of the materials are estimated from the high-frequency intercepts (marked in Fig. 4b).

The plots of the oxide-ion conductivities as a function of temperature for the compositions studied, in addition to that for the previously reported $Bi_2La_8[(GeO_4)_6]O_3$,[32] are shown in Fig. 4, while the conductivity values at 775 °C are compared in Table 5.
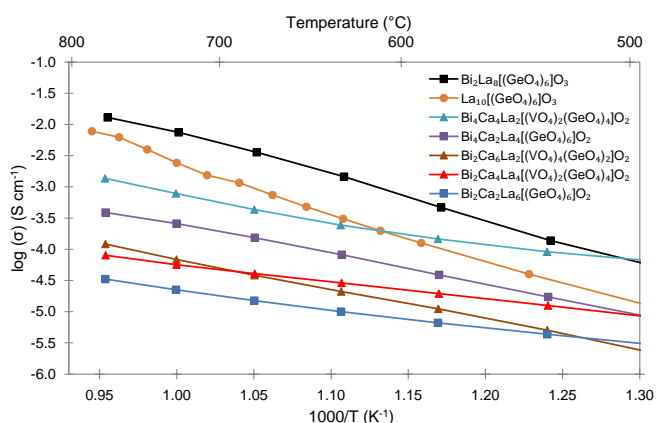

Fig. 5: Arrhenius plots of total conductivity values as a function of temperature for $Bi_2La_8[(GeO_4)_6]O_3$ and the related Bi(III)-containing apatite compounds studied.

Table 4: Conductivity values at 775 °C for the materials studied.

Composition	$\sigma_{775\,°C}$ (Scm^{-1})
$La_{10}[(GeO_4)_6]O_3$*	7.77×10^{-3}
$Bi_2La_8[(GeO_4)_6]O_3$	1.29×10^{-2}
$Bi_2Ca_4La_4[(VO_4)_2(GeO_4)_4]O_2$	8.04×10^{-5}
$Bi_2Ca_6La_2[(VO_4)_4(GeO_4)_2]O_2$	1.21×10^{-4}
$Bi_4Ca_4La_2[(VO_4)_2(GeO_4)_4]O_2$	1.37×10^{-3}
$Bi_2Ca_2La_6[(GeO_4)_6]O_2$	3.33×10^{-5}
$Bi_4Ca_2La_4[(GeO_4)_6]O_2$	3.89×10^{-4}

*785 °C

The materials studied are good oxide ion conductors, and the conductivity values measured reveal two trends. Firstly, as expected, the materials which contain extra interstitial oxygen (27 O atoms per formula unit) generally show higher conductivities than those with 26 O atoms per formula unit. The conductivities of $La_{10}[(GeO_4)_6]O_3$ and $Bi_2La_8[(GeO_4)_6]O_3$ are among the highest among the apatite-type materials . Secondly, within all three subsets of compositions, increasing the Bi content results in the increase of conductivity by up to an order of magnitude. The same trend has been found for the 800 °C conductivities of 5.5×10^{-5} Scm^{-1} and 1×10^{-3} Scm^{-1} reported for $La_8Ba_2[(GeO_4)_6]O_2$ and $La_6Bi_2Ba_2[(GeO_4)_6]O_2$, and 5.3×10^{-5} Scm^{-1}

and 3×10^{-3} Scm^{-1} reported for $La_8Sr_2[(GeO_4)_6]O_2$ and $La_6Bi_2Sr_2[(GeO_4)_6]O_2$.[4, 39]

Conclusions

In order to investigate the influence of lone-pair cations on the physical properties of apatite-type germanate oxide ion conductors, seven different compositions were prepared and characterised: the previously reported compositions $La_{10}[(GeO_4)_6]O_3$, $Bi_2La_8[(GeO_4)_6]O_3$, $Bi_2Ca_6La_2[(VO_4)_4(GeO_4)_2]O_2$, $Bi_2Ca_4La_4[(VO_4)_2(GeO_4)_4]O_2$, and $Bi_2Ca_2La_6[(GeO_4)_6]O_2$, and new compositions $Bi_4Ca_4La_2[(VO_4)_2(GeO_4)_4]O_2$ and $Bi_4Ca_2La_4[(GeO_4)_6]O_2$. The two new materials were structurally characterised by synchrotron X-ray and neutron diffraction, and the conductivities of all materials were determined by impedance spectroscopy. All materials are shown to be very good oxide ion conductors, stable in the temperature region investigated.

Crystallographic results demonstrate that the lone-pair containing Bi^{3+} shows a preference for the channel A-sites (A2 sites) in the apatite structure. Conductivity measurements reveal that increasing Bi^{3+} content leads to increases in conductivity by up to an order of magnitude. This is in agreement with the existing, albeit very sparse, literature on similar germanate apatites. This trend is, however, opposite to that found for the lanthanum silicate oxide-ion conductors with the apatite structure, which exhibit a dramatic decrease in conductivity on Bi(III) incorporation.[40] These results suggest significant differences in the oxide-ion conduction mechanisms in lone-pair containing apatite-type germanate and silicate solid electrolytes.

We have used a bond-valence energy landscape (BVEL) calculations method implemented in the 3DBVSMapper software[41, 42] for preliminary assessment of likely oxide-ion migration pathways in selected materials reported here. This method provides so-called "bond valence activation energy", which is a measure of the energy cost of connecting given crystallographic sites in the structure (via ionic migration), and as such can be used as a proxy, in relative terms, for the activation energy determined, for example, by impedance measurements. Calculations for $Bi_2La_8[(GeO_4)_6]O_3$ give values of 1.35 and 2.40 eV for the oxide ion migration through the apatite framework (via O^{2-} hopping between GeO_4 and GeO_5 units, which we have identified by neutron diffraction and electron microscopy[32]) and for direct migration down the apatite channel, respectively. Similar relative values for these two possible pathways have been calculated for $La_{10}[(GeO_4)_6]O_3$, $Bi_4Ca_2La_4[(GeO_4)_6]O_2$ and $Bi_4Ca_4La_2[(VO_4)_2(GeO_4)_4]O_2$. This is in contrast to the apatite-type silicate solid electrolytes, where computational studies have reported facile diffusion down the channels. [43]

In a separate strand of this project, we have recently been undertaking density functional theory (DFT) based molecular dynamics studies of a series of Bi(III)-containing apatite-type oxide ion conductors, which are expected to provide further and more explicit computational insight into the lone-pair effects observed experimentally and reported here.

Acknowledgements

Notes and references

1. P. R. Slater, J. E. H. Sansom and J. R. Tolchard, *Chemical Record*, 2004, **4**, 373-384.
2. A. Orera, T. Baikie, P. Panchmatia, T. J. White, J. Hanna, M. E. Smith, M. S. Islam, E. Kendrick and P. R. Slater, *Fuel Cells*, 2011, **11**, 10-16.
3. H. Li, T. Baikie, S. S. Pramana, J. F. Shin, P. R. Slater, F. Brink, J. Hester, K. Wallwork and T. J. White, *Journal of Materials Chemistry*, 2012 **22**, 2658-2669.
4. L. León-Reina, E. R. Losilla, M. Martinez-Lara, S. Bruque, A. Llobet, D. V. Sheptyakov and M. A. G. Aranda, *Journal of Materials Chemistry*, 2005, **15**, 2489-2498.
5. H. Zhang, F. Li, J. Jin, Q. Wang and Y. Sun, *Solid State Ionics*, 2008, **179**, 1024-1028.
6. H. Li, T. Baikie, S. S. Pramana, J. F. Shin, P. J. Keenan, P. R. Slater, F. Brink, J. Hester, T. An and T. J. White, *Inorganic Chemistry*, 2014, **53**, 4803-4812.
7. L. León-Reina, J. M. Porras-Vazquez, E. R. Losilla and M. A. G. Aranda, *Solid State Ionics*, 2006, **177**, 1307-1315.
8. J. McFarlane, S. Barth, M. Swaffer, J. E. H. Sansom and P. R. Slater, *Ionics*, 2002, **8**, 149-154.
9. S. P. Jiang, L. Zhang, H. Q. He, R. K. Yap and Y. Xiang, *Journal of Power Sources*, 2009, **189**, 972-981.
10. J. Xiang, Z.-G. Liu, J.-H. Ouyang and F.-Y. Yan, *Journal of Power Sources*, 2014, **251**, 305-310.
11. H. Yoshioka and S. Tanase, *Solid State Ionics*, 2005, **176**, 2395-2398.
12. J. E. H. Sansom and P. R. Slater, *Solid State Ionics*, 2004, **167**, 23-27.
13. L. León-Reina, E. R. Losilla, M. Martinez-Lara, M. C. Martin-Sedeno, S. Bruque, P. Nunez, D. V. Sheptyakov and M. A. G. Aranda, *Chemistry of Materials*, 2005, **17**, 596-600.
14. E. Kendrick, M. S. Islam and P. R. Slater, *Chemical Communications*, 2008, DOI: 10.1039/b716814d, 715-717.
15. M. S. Islam, J. R. Tolchard and P. R. Slater, *Chemical Communications*, 2003, DOI: 10.1039/b301179h, 1486-1487.
16. J. E. H. Sansom, D. Richings and P. R. Slater, *Solid State Ionics*, 2001, **139**, 205-210.
17. S. S. Pramana, W. T. Klooster and T. J. White, *Acta Cryst. B*, 2007, **63**, 597-602.
18. E. Kendrick, A. Orera and P. R. Slater, *Journal of Materials Chemistry*, 2009, **19**, 7955-7958.
19. R. Ali, M. Yashima, Y. Matsushita, H. Yoshioka, K. Ohoyama and F. Izumi, *Chemistry of Materials*, 2008, **20**, 5203-5208.
20. J. R. Tolchard and P. R. Slater, *Journal of Physics and Chemistry of Solids*, 2008, **69**, 2433-2439.
21. K. Imaizumi, K. Toyoura, A. Nakamura and K. Matsunaga, *Solid State Ionics*, 2014, **262**, 512-516.
22. K. Matsunaga and K. Toyoura, *Journal of Materials Chemistry*, 2012, **22**, 7265-7273.
23. T. An, T. Baikie, A. Orera, R. O. Piltz, M. Meven, P. R. Slater, J. Wei, M. L. Sanjuán and T. J. White, *Journal of the American Chemical Society*, 2016, **138**, 4468-4483.
24. P. M. Panchmatia, A. Orera, G. J. Rees, M. E. Smith, J. V. Hanna, P. R. Slater and M. S. Islam, *Angewandte Chemie International Edition*, 2011, **50**, 9328-9333.
25. Y. Nojiri, S. Tanase, M. Iwasa, H. Yoshioka, Y. Matsumura and T. Sakai, *Journal of Power Sources*, 2010, **195**, 4059-4064.
26. X. J. Kuang, Y. D. Li, C. D. Ling, R. L. Withers and I. R. Evans, *Chemistry of Materials*, 2010, **22**, 4484-4494.
27. X. J. Kuang, J. L. Payne, J. D. Farrell, M. R. Johnson and I. R. Evans, *Chemistry of Materials*, 2012, **24**, 2162-2167.
28. X. J. Kuang, J. L. Payne, M. R. Johnson and I. R. Evans, *Angewandte Chemie International Edition*, 2012, **51**, 690-694.
29. E. D. Wachsman, S. Boyapati, M. J. Kaufman and N. X. Jiang, *Journal of the American Ceramic Society*, 2000, **83**, 1964-1968.
30. E. D. Wachsman and K. T. Lee, *Science*, 2011, **334**, 935-939.
31. V. D. Zhuravlev, A. P. Tyutyunnik, V. G. Zubkov, L. A. Perelyaeva, I. V. Baklanova and A. L. Blinova, *Journal of Solid State Chemistry*, 2012, **194**, 32-36.
32. M. L. Tate, D. A. Blom, M. Avdeev, H. E. A. Brand, G. J. McIntyre, T. Vogt and I. R. Evans, *Advanced Functional Materials*, 2017, **27**.
33. K. S. Wallwork, B. J. Kennedy and D. Wang, *AIP Conference Proceedings*, 2007, **879**, 879-882.
34. K.-D. Liss, B. Hunter, M. Hagen, T. Noakes and S. Kennedy, *Physica B: Condensed Matter*, 2006, **385–386, Part 2**, 1010-1012.
35. A. A. Coelho, J. S. O. Evans, I. R. Evans, A. Kern and S. Parsons, *Powder Diffraction*, 2011, **26**, S22-S25.
36. H. M. Rietveld, *Journal of Applied Crystallography*, 1969, **2**, 65-71.
37. J. F. Huang and A. W. Sleight, *Journal of Solid State Chemistry*, 1993, **104**, 52-58.
38. J. T. S. Irvine, D. C. Sinclair and A. R. West, *Advanced Materials*, 1990, **2**, 132-138.
39. J. R. Tolchard, J. E. H. Sansom, P. R. Slater and M. S. Islam, *Journal of Solid State Electrochemistry*, 2004, **8**, 668-673.
40. E. Kendrick, M. S. Islam and P. R. Slater, *Journal of Materials Chemistry*, 2007, **17**, 3104-3111.
41. S. Adams, *Solid State Ionics*, 2006, **177**, 1625-1630.
42. M. Sale and M. Avdeev, *Journal of Applied Crystallography*, 2012, **45**, 1054-1056.
43. J. R. Tolchard, M. S. Islam and P. R. Slater, *Journal of Materials Chemistry*, 2003, **13**, 1956-1961.